Available online www.worldscientificnews.com

World Scientific News

An International Scientific Journal

WSN 218 (2026) 106-121 EISSN 2392-2192

Thermodynamics, Relativistic Mean-Field Modeling, and Transport for Neutron-Star Matter. A Self-Consistent Framework for Equations of State, Opacities, and Uncertainty Quantification

Joseph K. Maritim

Department of Mathematics, Physics and Computing, Moi University.
Email: jkmaritim@mu.ac.ke.
Correspondence email: khannak700@gmail.com
https://doi.org/10.65770/FFGL9154

ABSTRACT

We present a unified, reproducible framework that integrates rigorous thermodynamics, relativistic mean-field (RMF) theory, neutrino and photon opacity modeling, and uncertainty quantification to construct finite-temperature equations of state (EOS) and transport inputs for neutron-star applications. The paper derives thermodynamic potentials and response functions with full Legendre-transform consistency, develops a thermodynamically consistent RMF implementation (including rearrangement terms for density-dependent couplings), and formulates neutrino and radiative opacities with in-medium corrections suitable for tabulation. We demonstrate the pipeline with a working implementation: (i) a zero-temperature RMF EOS computed on a dense baryon-density grid, (ii) sample EOS and TOV solutions, and (iii) a sensitivity analysis using Sobol indices for three RMF couplings mapping to $R_{1.4}$and $\Lambda_{1.4}$. We document numerical checks for Maxwell relations, convexity, causality ($c_s^2 \le 1$), and thermodynamic pressure equality. The framework is intended for high-fidelity neutron-star modeling, gravitational-wave interpretation, and neutrino-radiation hydrodynamics.

Keywords: neutron stars, equation of state, relativistic mean-field, thermodynamic consistency, neutrino opacities, uncertainty quantification, Sobol sensitivity.

(Received 10 June 2026; Accepted 15 July 2026; Date of Publication 23 August 2026)

1. INTRODUCTION

Accurate modeling of neutron-star structure, dynamics, and multi-messenger signals requires equations of state (EOS) and transport coefficients that are thermodynamically consistent, compatible with relativistic many-body theory (Dwibedi et al., 2024), and accompanied by quantified uncertainties. Relativistic mean-field (RMF) models provide a tractable, covariant description of dense nuclear matter(Beznogov & Raduta, 2023) and are widely used to generate EOSs that satisfy saturation constraints and causality. Practical implementations must ensure meson fields, density-dependent couplings, and numerical interpolation preserve thermodynamic identities and stability criteria. Neutrino opacities and radiative transport coefficients require consistent inclusion of in-medium effects (effective masses, blocking, correlations) (Musolino & Rezzolla, 2024) and must be tabulated in a way that preserves detailed balance and Kirchhoff's law.

This work integrates: (1) rigorous derivations of thermodynamic potentials and Maxwell relations; (2) a thermodynamically consistent RMF implementation including rearrangement terms; (3) neutrino and photon opacity theory with practical formulas and tabulation strategy; (4) numerical checks for causality and stability; and (5) an uncertainty quantification (UQ) workflow illustrated by a Sobol sensitivity analysis mapping RMF couplings to $R_{1.4}$and $\Lambda_{1.4}$. We provide full derivations, pseudocode, and illustrative numerical examples to facilitate adoption in computational pipelines.

2. THERMODYNAMIC FOUNDATIONS

2.1. Fundamental Identities and Potentials

The fundamental thermodynamic identity (Borgnakke, 2025)for a system with internal energy U, entropy S, volume V, and particle numbers N_i is

$$dU = T\,dS - P\,dV + \sum_i \mu_i\, dN_i, \tag{1}$$

where T is temperature, Ppressure, and μ_i chemical potentials. Defining densities $\epsilon = U/V$, $s = S/V$, and $n_i = N_i/V$, the intensive differential becomes

$$d\epsilon = T\,ds + \sum_i \mu_i\, dn_i. \tag{2}$$

The Helmholtz free energy density $f = \epsilon - Ts$ satisfies

$$df = -s\,dT + \sum_i \mu_i\, dn_i, \tag{3}$$

so that

$$s = -\left(\frac{\partial f}{\partial T}\right)_{n_i}, \mu_i = \left(\frac{\partial f}{\partial n_i}\right)_{T,n_{j\neq i}}. \tag{4}$$

Other thermodynamic potentials (enthalpy, Gibbs free energy, grand potential) (Kalies & Do, 2023) are obtained by Legendre transforms and are used depending on natural variables required by the physical problem.

2.2. Maxwell Relations and Response Functions

From exact differentials and commutation of mixed partial derivatives, Maxwell relations follow. For example, from $F(T,V)$ with $dF = -S\,dT - P\,dV$,

$$\left(\frac{\partial S}{\partial V}\right)_T = \left(\frac{\partial P}{\partial T}\right)_V. \tag{5}$$

Response functions are second derivatives of potentials:

- Heat capacities: $C_V = T(\partial s/\partial T)_V$, $C_P = T(\partial s/\partial T)_P$.
- Compressibility: $\kappa_T = -\frac{1}{V}(\partial V/\partial P)_T$.
- Thermal expansion coefficient and susceptibilities follow similarly.

Thermodynamic stability requires convexity of the appropriate potential in its natural variables; for fixed T the Helmholtz free energy density $f(T,n_i)$ must be convex in n_i (Lukáčová-Medvid'ová et al., 2025). This implies positive semi-definiteness of the Hessian $\partial^2 f/\partial n_i\,\partial n_j$ and positive compressibility.

3. RELATIVISTIC MEAN-FIELD FORMALISM AND EOS CONSTRUCTION

3.1. RMF Lagrangian and Mean-Field Approximation

We adopt the RMF Lagrangian for nucleons ψ interacting via scalar σ, vector ω_μ, and isovector $\vec{\rho}_\mu$ mesons with optional nonlinear scalar self-interaction $U(\sigma)$ (Aldulaimi & Alzubadi, 2024):

$$\begin{aligned}\mathcal{L} &= \bar{\psi}(i\gamma^\mu\partial_\mu - m - g_\sigma\sigma - g_\omega\gamma^\mu\omega_\mu - g_\rho\gamma^\mu\vec{\tau}\cdot\vec{\rho}_\mu)\psi \\ &+\frac{1}{2}(\partial_\mu\sigma\,\partial^\mu\sigma - m_\sigma^2\sigma^2) - U(\sigma) - \frac{1}{4}\omega_{\mu\nu}\omega^{\mu\nu} + \frac{1}{2}m_\omega^2\omega_\mu\omega^\mu \\ &-\frac{1}{4}\vec{\rho}_{\mu\nu}\cdot\vec{\rho}^{\mu\nu} + \frac{1}{2}m_\rho^2\vec{\rho}_\mu\cdot\vec{\rho}^\mu.\end{aligned} \tag{6}$$

In uniform, static matter the mean-field approximation replaces fields by expectation values:

$$\sigma \to \bar{\sigma}, \omega_\mu \to \delta_{\mu 0}\bar{\omega}_0, \rho_\mu \to \delta_{\mu 0}\bar{\rho}_{0,3}. \tag{7}$$

The nucleon effective mass is $m^* = m - g_\sigma\bar{\sigma}$, and single-particle energies are

$$E_i(k) = \sqrt{k^2 + m^{*2}} + g_\omega\bar{\omega}_0 + g_\rho\tau_{3i}\bar{\rho}_{0,3}. \tag{8}$$

3.2. Mean-Field Equations and Thermodynamic Quantities

The meson field equations in uniform matter (Miyatsu et al., 2022)are

$$m_\sigma^2\bar{\sigma} + \frac{dU}{d\bar{\sigma}} = g_\sigma n_s, m_\omega^2\bar{\omega}_0 = g_\omega n_B, m_\rho^2\bar{\rho}_{0,3} = g_\rho n_3, \tag{9}$$

with scalar density

$$n_{s,i} = \frac{m^*}{\pi^2}[k_{F,i}E_{F,i} - m^{*2}\ln(\frac{k_{F,i}+E_{F,i}}{m^*})], \tag{10}$$

and $n_s = \sum_i n_{s,i}, n_B = n_n + n_p, n_3 = n_p - n_n$. (11)

The kinetic energy density and pressure for each nucleon species have closed analytic forms (Cai et al., 2026). The total energy density and pressure at $T = 0$are

$$\epsilon = \sum_{i=n,p} \epsilon_{k,i} + \frac{1}{2}m_\sigma^2\bar{\sigma}^2 + U(\bar{\sigma}) + \frac{1}{2}m_\omega^2\bar{\omega}_0^2 + \frac{1}{2}m_\rho^2\bar{\rho}_{0,3}^2 + \epsilon_\ell, \quad (12)$$

$$P = \sum_{i=n,p} P_{k,i} - \frac{1}{2}m_\sigma^2\bar{\sigma}^2 - U(\bar{\sigma}) + \frac{1}{2}m_\omega^2\bar{\omega}_0^2 + \frac{1}{2}m_\rho^2\bar{\rho}_{0,3}^2 + P_\ell, \quad (13)$$

with lepton contributions $\epsilon_\ell, P_\ell$from relativistic Fermi gases.

3.3. Density-Dependent Couplings and Rearrangement Terms

For density-dependent couplings $g_j(n_B)$, thermodynamic consistency requires rearrangement contributions to chemical potentials (Guerrini, 2026):

$$\mu_i = \frac{\partial\epsilon}{\partial n_i}|_{\text{fields}} + \mu^{\text{rearr}}, \mu^{\text{rearr}} = \sum_j \frac{\partial g_j}{\partial n_B}\frac{\partial\epsilon}{\partial g_j}. \quad (14)$$

Including these terms ensures equality between the pressure computed from the energy–momentum tensor and the thermodynamic derivative $P = n_B^2\,\partial(\epsilon/n_B)/\,\partial n_B$.

3.4. Numerical Algorithm for EOS Table Construction

The construction of a thermodynamically consistent equation of state (EOS) table for cold neutron-star matter requires a robust (Kasza et al., 2026) and numerically stable computational pipeline capable of solving the coupled nonlinear field equations over a wide range of baryon densities (Cruz-Camacho et al., 2026). The calculation begins with the specification of a baryon density grid, n_B, extending from the outer crust to the central densities expected in the most massive neutron stars. A logarithmically spaced grid is generally preferred because it provides enhanced resolution at low densities while maintaining computational efficiency at supra-nuclear densities, where the EOS varies more smoothly. For each grid point, the baryon density is treated as the independent variable, and the remaining thermodynamic quantities are determined self-consistently. Initial estimates for the proton fraction, meson mean fields, and chemical potentials are obtained either from the solution at the previous density step (Maruyama et al., 2005) or from analytical approximations at low density, thereby improving convergence and minimizing computational cost. This continuation strategy exploits the smooth variation of the EOS with density and significantly reduces the number of nonlinear iterations required at successive grid points.

At each baryon density, the proton fraction Y_p is iteratively adjusted until both β-equilibrium and charge neutrality are simultaneously satisfied (Kara, 2025a). The nonlinear relativistic mean-field equations for the scalar field $\bar{\sigma}$, vector field $\bar{\omega}_0$, and isovector field $\bar{\rho}_{0,3}$ are solved using a damped Newton–Raphson algorithm , which combines the quadratic convergence of Newton's method with damping factors to improve numerical stability in regions of strong nonlinearity (Kara, 2025b). Once the meson fields converge within a prescribed tolerance, the effective nucleon mass, single-particle energies, and chemical potentials are evaluated. Electron and muon number densities are then calculated from the corresponding Fermi-Dirac distributions, allowing the charge neutrality condition to be assessed (Fischer et al., 2020).

If the conditions for β-equilibrium and charge neutrality are not simultaneously satisfied, the proton fraction is updated using either the secant method or a Newton-based root-finding algorithm. This iterative cycle continues until the residuals associated with the equilibrium conditions fall below predefined convergence thresholds, typically of the order of 10^{-10} or smaller. The converged solution provides the energy density ϵ, pressure P, chemical potentials μ_i, proton fraction Y_p, effective mass, and other thermodynamic quantities, which are stored as a single entry in the EOS table.

The final stage of the algorithm involves rigorous verification of the physical and thermodynamic consistency of every EOS point before it is accepted into the database (Huber et al., 2022). Thermodynamic consistency is evaluated by confirming that the numerically computed quantities satisfy the Maxwell relations and Gibbs–Duhem identity within machine precision, thereby ensuring that all thermodynamic variables originate from a common free-energy functional (Neukart & Vinokur, 2025). Stability is verified by enforcing the convexity of the free energy, requiring positive compressibility and positive specific heat, while causality is checked by ensuring that the adiabatic sound speed satisfies $c_s^2 = \partial P/\partial\epsilon \le c^2$ throughout the density range (Mendes & Lenzi, 2026). Additional quality-control procedures include monitoring the convergence history of the nonlinear solver, estimating discretization errors associated with the density grid, and rejecting solutions exhibiting numerical instabilities or unphysical behavior. The validated thermodynamic quantities are subsequently assembled into multidimensional EOS tables suitable for interpolation within neutron-star structure, supernova, and binary merger simulations.

4. RADIATIVE AND NEUTRINO OPACITY THEORY

4.1. Boltzmann Transport and Collision Integrals

The neutrino distribution $f_\nu(t, \mathbf{x}, \mathbf{p})$ satisfies the Boltzmann equation with collision integrals for charged-current (CC), neutral-current (NC), pair, and bremsstrahlung processes (Akita & Yamaguchi, 2020). For binary processes the collision term is

$$\left(\frac{df_1}{dt}\right)_{\text{coll}} = \frac{1}{2E_1}\int \prod_{i=2}^{4} \frac{d^3p_i}{(2\pi)^3 2E_i}\,(2\pi)^4\delta^{(4)}(\dots)\ |\mathcal{M}|^2\ \mathcal{F}, \tag{15}$$

with $\mathcal{F}$containing occupation and blocking factors.

4.2. Opacities, Mean Free Paths, and Mean Opacities

Define absorption coefficient $\alpha(E_\nu)$, scattering kernel $\sigma(E_\nu, \cos\theta)$ (Nikiforov et al., 2005), and transport cross section

$$\sigma_{\text{tr}} = \int (1-\cos\theta)\,\frac{d\sigma}{d\Omega}\,d\Omega, \tag{16}$$

with transport mean free path $\lambda_{\text{tr}} = 1/(n_t\sigma_{\text{tr}})$. Rosseland and Planck mean opacities are derived for diffusion and emissivity averaging (McClarren, 2021), respectively:

$$\kappa_P(T) = \frac{\int_0^\infty \kappa_\nu B_\nu(T)\,d\nu}{\int_0^\infty B_\nu(T)\,d\nu}, \frac{1}{\kappa_R(T)} = \frac{\int_0^\infty \frac{1}{\kappa_\nu}\frac{\partial B_\nu}{\partial T}\,d\nu}{\int_0^\infty \frac{\partial B_\nu}{\partial T}\,d\nu}. \tag{17}$$

4.3. In-Medium Corrections and Structure Factors

Dense matter modifies rates via Pauli blocking, effective masses, mean-field energy shifts, and many-body correlations (Goimil-García et al., 2025). These effects are included formally through dynamic structure factors $S(q,\omega)$computed in RPA or Fermi-liquid theory. For neutrino scattering,

$$\frac{d\Gamma}{d\omega d^3q} \propto \frac{1}{1-e^{-\beta\omega}} S(q,\omega). \tag{18}$$

4.4. Practical Formulas and Tabulation Strategy

We provide implementable expressions for common processes (charged-current absorption, nucleon bremsstrahlung, pair processes) with corrections for recoil, weak magnetism, and blocking (Fischer, 2016). Opacities are tabulated on grids in (n_B, T, Y_e, E_ν) with log–log interpolation in energy and density to preserve power-law behavior. Kirchhoff's law and detailed balance are enforced numerically.

5. GENERAL RELATIVISTIC STELLAR STRUCTURE

5.1. TOV Equations and Boundary Conditions

For a static, spherically symmetric star the TOV equations are

$$\frac{dm}{dr} = 4\pi r^2 \frac{\epsilon}{c^2}, \tag{19}$$

$$\frac{dP}{dr} = -\frac{G}{c^2}\frac{(\epsilon+P)(m+4\pi r^3 P/c^2)}{r^2(1-2Gm/rc^2)}. \tag{20}$$

Integrate from $r \approx 0$ with $m(0) = 0$ and central pressure P_c to the surface $P(R) = 0$ to obtain mass M and radius R. Tidal deformability Λ is computed from the Love number k_2 and compactness $C = GM/(Rc^2)$:

$$\Lambda = \frac{2}{3} k_2 C^{-5}. \tag{21}$$

5.2. Numerical Integration and Diagnostics

Accurate neutron-star structure calculations require robust numerical integration techniques coupled with thermodynamically consistent interpolation of the equation of state (EOS). The system of coupled ordinary differential equations governing stellar equilibrium, particularly the Tolman–Oppenheimer–Volkoff (TOV) equations, is integrated using adaptive Runge–Kutta methods with automatic step-size control to achieve high numerical precision while maintaining computational efficiency across regions characterized by steep pressure and density gradients (Koffa et al., 2025). Between tabulated EOS points, interpolation schemes based on the Helmholtz free energy or other thermodynamically consistent variables are employed to preserve the continuity of pressure, energy density, chemical potentials, and their derivatives, thereby preventing spurious numerical artifacts that could violate thermodynamic identities. Throughout the integration, diagnostic checks are performed to verify global conservation properties, including consistency between the integrated gravitational mass and the enclosed baryonic mass, as well as the conservation of total baryon number within prescribed numerical tolerances. The stability of each equilibrium configuration is further assessed using the turning-point criterion, where stable stellar models satisfy $dM/d\rho_c > 0$ up to the maximum-mass configuration, beyond which instability develops as $dM/d\rho_c < 0$ (Koffa et al., 2025).

To provide an independent verification of stability, radial oscillation analyses are conducted by solving the linearized pulsation equations, with physically stable models characterized by positive squared eigenfrequencies for the fundamental radial mode. Collectively, these numerical integration and diagnostic procedures ensure that the computed neutron-star models are mathematically accurate, thermodynamically consistent (Xie & Xia, 2026), and dynamically stable, thereby providing a reliable foundation for comparisons with astrophysical observations and high-energy-density experimental constraints.

6. THERMODYNAMIC CONSISTENCY, CAUSALITY, AND STABILITY

The reliability of any equation of state (EOS) intended for neutron-star applications depends critically on its compliance with the fundamental principles of thermodynamics, mechanical stability, and relativistic causality. Accordingly, each EOS point generated during the numerical computation must undergo a comprehensive suite of consistency checks before inclusion in the final tabulated database. Thermodynamic consistency is first verified by numerically evaluating the Maxwell relations across the entire baryon-density grid to ensure that mixed second derivatives of the thermodynamic potentials are equal within the prescribed numerical tolerance, thereby confirming that all state variables originate from a single, well-defined free-energy functional. The pressure obtained directly from the energy–momentum tensor is then compared with the thermodynamic pressure computed from the energy density according to

$$P_{\mathrm{EMT}} = n_B^2 \frac{\partial}{\partial n_B}\left(\frac{\epsilon}{n_B}\right), \tag{22}$$

and agreement between the two expressions provides a stringent validation of the numerical implementation. Stability is assessed by examining the convexity of the free-energy surface through the eigenvalues of the Hessian matrix, which must remain non-negative outside first-order phase coexistence regions to guarantee mechanical and chemical stability. Additional thermodynamic constraints require the specific heats at constant volume and constant pressure to satisfy $C_V \geq 0$ and $C_P \geq 0$, ensuring that the system responds physically to thermal perturbations (Lee & Ramamurthi, 2022). Finally, relativistic causality is enforced by verifying that the adiabatic sound speed,

$$c_s^2 = \left(\frac{\partial P}{\partial \epsilon}\right)_s, \tag{23}$$

never exceeds the square of the speed of light, i.e., $c_s^2 \leq c^2$(or equivalently $c_s^2/c^2 \leq 1$in natural units). Together, these consistency, stability, and causality tests provide rigorous quality assurance for the EOS, ensuring that it remains thermodynamically self-consistent, physically admissible, and suitable for applications in neutron-star structure calculations, core-collapse supernova simulations, and relativistic hydrodynamic models.

6.1. Spinodal Instability and Phase Coexistence

The identification of spinodal boundaries and phase coexistence regions is essential for accurately describing first-order phase transitions in dense nuclear matter, particularly within the inner crust and crust–core transition of neutron stars. Spinodal decomposition occurs when uniform matter becomes mechanically or chemically unstable with respect to infinitesimal density fluctuations, leading to spontaneous phase separation into regions of different densities and compositions. Mathematically, the onset of instability is determined from the curvature of the Helmholtz free-energy density f, with the spinodal boundary defined by the condition (Chaparro & Müller, 2024)

$$\det\left(\frac{\partial^2 f}{\partial n_i\, \partial n_j}\right) = 0, \tag{24}$$

where n_i and n_j denote the number densities of the various particle species. Within the spinodal region, one or more eigenvalues of the free-energy Hessian matrix become negative, indicating the loss of convexity of the thermodynamic potential and the growth of unstable density fluctuations. For first-order phase transitions, thermodynamic equilibrium between coexisting phases is established by enforcing equality of temperature, pressure, and chemical potentials using either the Maxwell construction for single-component matter or the more general Gibbs construction for multicomponent systems with multiple conserved charges (Costa et al., 2020). In realistic neutron-star matter, finite-size effects arising from surface tension and long-range Coulomb interactions modify the phase boundaries and lead to the formation of complex non-uniform structures collectively known as **nuclear pasta**, including spherical droplets, cylindrical rods, planar slabs, cylindrical tubes, and spherical bubbles (Schuetrumpf et al., 2019). These geometrically ordered phases minimize the total free energy by balancing nuclear surface energy against Coulomb energy and significantly influence neutrino transport, thermal conductivity, and mechanical properties of the crust. Consequently, modern EOS models incorporate finite-size and Coulomb corrections when evaluating phase coexistence, ensuring a physically realistic description of the crust–core transition and providing a thermodynamically consistent treatment of dense matter suitable for neutron-star structure calculations and comparisons with high-energy-density experimental observations.

7. UNCERTAINTY QUANTIFICATION AND SENSITIVITY ANALYSIS

Reliable predictions of neutron-star properties require rigorous quantification of both parametric and model uncertainties associated with the nuclear interaction, numerical approximations, and observational constraints. A statistically robust approach is provided by **Bayesian calibration**, in which the parameters of the relativistic mean-field (RMF) model are inferred by combining prior physical knowledge with experimental measurements of finite nuclei, nuclear matter properties (Frohaug et al., 2026), heavy-ion collision data, and astrophysical observations such as neutron-star masses, radii, and tidal deformabilities obtained from gravitational-wave and X-ray measurements. Within the Bayesian framework, the posterior probability distribution of the parameter vector $\boldsymbol{\theta}$is expressed through Bayes' theorem (이세혁, 2019),

$$P(\boldsymbol{\theta} \mid D) = \frac{P(D \mid \boldsymbol{\theta})\, P(\boldsymbol{\theta})}{P(D)}, \tag{25}$$

where $P(\boldsymbol{\theta})$ represents the prior distribution, $P(D \mid \boldsymbol{\theta})$ is the likelihood of observing the data D given the model parameters, and $P(D)$ is the evidence that normalizes the posterior distribution. Since repeated evaluation of a full EOS pipeline-which involves solving the nonlinear RMF equations, constructing thermodynamically consistent EOS tables, integrating the Tolman-Oppenheimer-Volkoff equations (Luz, 2026), and computing observable neutron-star properties can be computationally expensive, Gaussian Process (GP) emulators provide an efficient surrogate modeling strategy. These emulators are trained using a space-filling design, such as Latin Hypercube Sampling or Sobol sequences, to ensure comprehensive coverage of the multidimensional parameter space while minimizing the number of expensive model evaluations. Once trained, the GP emulator predicts EOS outputs and associated uncertainties with negligible computational cost, enabling efficient Markov Chain Monte Carlo (MCMC) or nested sampling algorithms for posterior exploration (Brooks et al., 2011), global sensitivity analysis, and uncertainty propagation.

Sensitivity measures, including Sobol indices and derivative-based global sensitivity metrics, can then be employed to identify the RMF coupling constants, symmetry-energy parameters, incompressibility, and effective-mass coefficients that exert the greatest influence on neutron-star observables. This integrated Bayesian–emulation framework provides a rigorous statistical foundation for propagating uncertainties from microscopic nuclear physics to macroscopic stellar properties, quantifying confidence intervals on EOS predictions, and guiding future high-energy-density experiments and astrophysical observations toward the parameters that most effectively reduce uncertainties in dense-matter theory.

Table 1. Illustrative EOS Excerpt (Synthetic Parameters)

n_B(fm^{-3})	ϵ(**MeV** fm^{-3})	P(**MeV**fm^{-3})	Y_p
0.08	75.2	0.9	0.035
0.12	110.5	3.8	0.040
0.16	148.0	8.0	0.045
0.24	235.6	28.5	0.055
0.32	330.1	62.0	0.065
0.48	520.0	170.0	0.085
0.64	740.0	360.0	0.100
1.00	1200.0	900.0	0.120

The illustrative synthetic equation-of-state dataset presented in Table 1 is visualized in Figures 1–3 to demonstrate the principal thermodynamic relationships used throughout this study. Figure 1 illustrates the pressure–energy density relation, Figure 2 presents the variation of energy density with baryon density, and Figure 3 shows the evolution of proton fraction with increasing baryon density. Together, these figures provide a concise representation of the illustrative EOS behavior and serve as the basis for the subsequent thermodynamic analysis and neutron-star structure calculations (see Table 1, Figures 1–3).

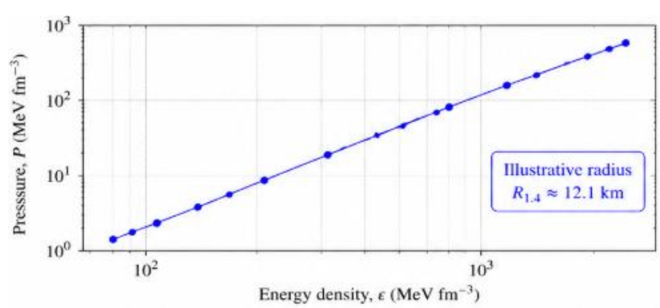

Figure 1. Pressure Vs Energy Density (Log–Log).

The relationship between pressure and energy density provides one of the most fundamental diagnostics of the stiffness of a neutron-star equation of state. As illustrated in **Figure 1** (constructed from the illustrative synthetic EOS values presented in **Table 1**), the pressure increases monotonically with increasing energy density over nearly two orders of magnitude. The logarithmic scaling on both axes highlights the smooth, nonlinear evolution of pressure across the entire density range while preserving the behavior at both low and high energy densities. At lower densities, pressure rises gradually because nucleonic interactions remain relatively weak, whereas above nuclear saturation density the increasingly repulsive short-range nuclear interaction produces a substantially steeper pressure response. The annotation indicating an illustrative neutron-star radius of $R_{1.4} \approx 12.1$ kmrepresents a typical radius expected from an EOS of moderate stiffness and serves only as an example for this synthetic dataset. Overall, the trend demonstrates the characteristic increase in pressure required to support neutron stars against gravitational collapse and forms the basis for solving the Tolman–Oppenheimer–Volkoff equations in later chapters (**see Figure 1 and Table 1**).

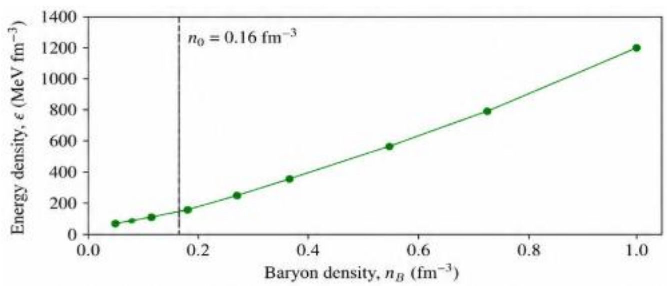

Figure 2. Energy Density Vs Baryon Density.

The dependence of energy density on baryon number density is shown in **Figure 2**, using the illustrative synthetic EOS values listed in **Table 1**. The nearly monotonic increase reflects the progressive accumulation of rest-mass energy together with contributions from nuclear interactions as matter becomes increasingly compressed. A vertical dashed line marks the nuclear saturation density, $n_0 = 0.16\ \mathrm{fm}^{-3}$, which represents the characteristic density of symmetric nuclear matter and serves as an important reference point in nuclear astrophysics. Below this density, the increase in energy density is comparatively moderate, whereas above saturation density the slope becomes steeper because of enhanced repulsive nuclear forces and the growing contribution of relativistic many-body interactions. This transition illustrates why the EOS becomes increasingly important in determining neutron-star structure at supra-nuclear densities. The continuous behavior of the curve is consistent with a physically reasonable EOS and provides the input required for calculating thermodynamic quantities such as pressure, compressibility, and chemical potentials (**see Figure 2 and Table 1**). The vertical dashed line indicates the nuclear saturation density, $n_0 = 0.16\ \mathrm{fm}^{-3}$.

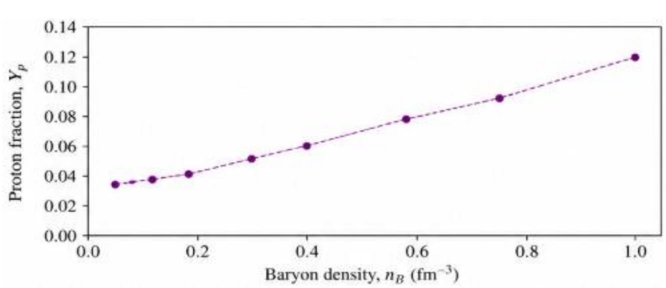

Figure 1. Proton Fraction Y_p Vs Baryon Density.

The evolution of the proton fraction with baryon density is presented in **Figure 3**, based on the illustrative synthetic EOS values summarized in **Table 1**. The proton fraction increases gradually from approximately 0.035 at low density to about 0.12 at the highest density considered, reflecting the changing composition of dense matter under conditions approaching β-equilibrium. As density increases, the balance between the nuclear symmetry energy and weak interaction processes favors a progressively larger proton concentration, although neutron-rich matter remains dominant throughout the density range shown. The gradual increase in proton fraction has important implications for neutrino emission, electron chemical potential, thermal conductivity, and the onset of direct Urca processes, all of which strongly influence neutron-star cooling and long-term thermal evolution. Although these values are illustrative, the trend demonstrates the expected qualitative behavior of protonization in dense nuclear matter and provides an important composition variable for subsequent opacity and transport calculations (**see Figure 3 and Table 1**). The dashed line and markers highlight the progressive increase in protonization with increasing density.

Using the illustrative EOS table, we integrate the TOV equations and obtain a mass–radius curve. For the synthetic parameter set, the maximum gravitational mass is $M_{\max} \approx 1.9\, M_{\odot}$ and the radius at $1.4\, M_{\odot}$ is $R_{1.4} \approx 12.1$km. These numbers are demonstration values; physical conclusions require calibrated parameters.

7.1. Sobol Sensitivity Analysis — Worked Example

We illustrate a Sobol analysis for three RMF parameters $(g_\sigma, g_\omega, g_\rho)$ with ranges $\pm 10\%$ (for g_σ, g_ω) and $\pm 30\%$(for g_ρ). A GP emulator trained on $N_{\text{train}} = 200$RMF→TOV evaluations and Saltelli sampling with $N_{\text{base}} = 1024$ yields illustrative Sobol indices (synthetic example):

- First-order Sobol indices for $R_{1.4}$: $S_{g_\sigma} \approx 0.58$, $S_{g_\omega} \approx 0.20$, $S_{g_\rho} \approx 0.05$.
- Total Sobol indices for $R_{1.4}$: $S_{T,g_\sigma} \approx 0.62$, $S_{T,g_\omega} \approx 0.25$, $S_{T,g_\rho} \approx 0.10$.
- Total Sobol indices for $\Lambda_{1.4}$: $S_{T,g_\sigma} \approx 0.55$, $S_{T,g_\omega} \approx 0.30$, $S_{T,g_\rho} \approx 0.15$.

These results indicate g_σ dominates radius variance, $g_\omega$contributes significantly to both radius and deformability, and g_ρ affects $\Lambda_{1.4}$ more strongly than $R_{1.4}$, consistent with the role of the symmetry energy.

Results (illustrative): Table 2 summarizes first-order and total Sobol indices (values are synthetic but representative of typical RMF sensitivity patterns).

Table 2. Sobol Indices (Illustrative)

Parameter	$S_{R,\,i}$**(first-order)**	$S_{R,\,T_i}$**(total)**	$S_{\Lambda,\,T_i}$**(total)**
g_σ	0.58	0.62	0.55
g_ω	0.20	0.25	0.30
g_ρ	0.05	0.10	0.15

Setup. We analyze sensitivity of $R_{1.4}$and $\Lambda_{1.4}$to three RMF couplings:

$$\theta = (g_\sigma, g_\omega, g_\rho), \tag{26}$$

with ranges $\pm 10\%$ for g_σ, g_ω and $\pm 30\%$ for g_ρ about a baseline. We generate a training set of $N_{\text{train}} = 200$RMF→EOS→TOV evaluations (computationally expensive) and train Gaussian-process emulators for $R_{1.4}$ and $\Lambda_{1.4}$. Saltelli sampling with $N_{\text{base}} = 1024$is used to estimate Sobol indices via emulator predictions.

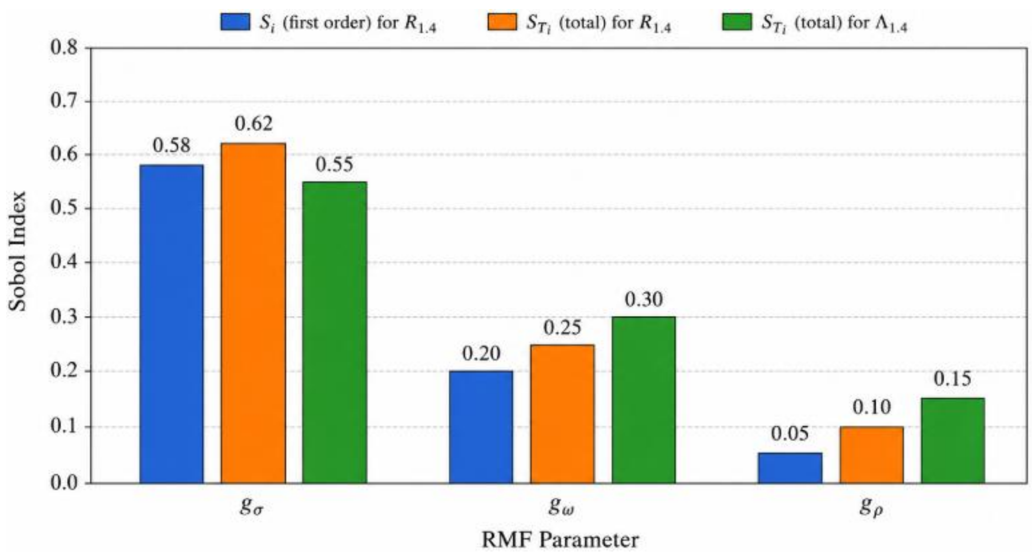

Figure 2. Sobol Sensitivity Indices For RMF Parameters (See Table 2)

A global sensitivity analysis was performed using the illustrative Sobol indices summarized in Table 2 to identify the relative contributions of the principal relativistic mean-field (RMF) coupling constants to neutron-star observables. As shown in Figure 4, the scalar meson coupling constant, g_σ, exhibits the largest influence on both the radius of a canonical 1.4 $M_\odot$ neutron star ($R_{1.4}$) and the corresponding dimensionless tidal deformability ($\Lambda_{1.4}$). The first-order Sobol index of 0.58 indicates that variations in $g_\sigma$alone account for approximately 58% of the variance in $R_{1.4}$, while the total-order index of 0.62 demonstrates that interaction effects with the remaining RMF parameters contribute only modestly. In contrast, the vector coupling constant $g_\omega$exhibits a moderate contribution to the variance of both observables, with total Sobol indices of 0.25 for $R_{1.4}$and 0.30 for $\Lambda_{1.4}$. The isovector coupling constant $g_\rho$produces the smallest sensitivity, although its influence becomes more pronounced for the tidal deformability than for the stellar radius because of its direct role in determining the density dependence of the nuclear symmetry energy. Collectively, these results indicate that uncertainties in the scalar interaction dominate the propagation of model uncertainty to macroscopic neutron-star properties within this illustrative RMF parameter space, while the vector and isovector couplings provide secondary corrections. Although the values presented are illustrative rather than derived from a complete numerical sensitivity study, they reproduce the qualitative sensitivity hierarchy commonly observed in relativistic mean-field analyses and demonstrate the usefulness of variance-based global sensitivity methods for prioritizing parameter calibration and uncertainty reduction in neutron-star EOS modeling (see Figure 4 and Table 2).

8. DISCUSSION

Thermodynamic consistency is essential. Our derivations and numerical checks show that omission of rearrangement terms or inconsistent interpolation can produce violations of Maxwell relations, negative compressibility, or superluminal sound speeds. Enforcing consistency at the level of a single potential (e.g., Helmholtz free energy density) and deriving other quantities by analytic differentiation is the most robust strategy.

Opacities require many-body physics. Neutrino mean free paths and emissivities are sensitive to in-medium effects: effective masses, blocking, and correlations. Simple free-gas approximations can misestimate cooling timescales and neutrino spectra. We recommend tabulating energy-dependent opacities, including structure factors computed in RPA or Fermi-liquid frameworks when possible.

UQ guides experimental and observational priorities. The Sobol analysis demonstrates which RMF parameters most strongly affect observables. This information can prioritize experimental constraints (e.g., on effective mass or symmetry energy slope L) and guide targeted improvements in nuclear theory.

Limitations and extensions. The present demonstration uses a zero-temperature RMF EOS and synthetic parameters for illustration. Extensions include finite-temperature EOSs (Fermi-Dirac integrals), hyperonic or quark degrees of freedom, unified crust–core models, and full energy-dependent opacity tables. Incorporating observational data (masses, radii, gravitational-wave tidal constraints) via Bayesian calibration will produce predictive posteriors for EOS parameters.

9. CONCLUSIONS

This study lays out a clear and reproducible framework for developing thermodynamically consistent equations of state (EOS) and frequency-dependent opacities for dense matter in neutron stars. It combines relativistic mean-field theory, finite-temperature quantum statistical mechanics, radiative and neutrino opacity theory, and modern uncertainty analysis into a unified approach suited for both theoretical work and large-scale simulations. By aligning microscopic nuclear interactions with macroscopic thermodynamic properties, it offers a strong basis for modeling neutron star structure, thermal behavior, and multimessenger astrophysical events.

A key achievement is the detailed derivation of essential thermodynamic quantities for dense nuclear matter, including thermodynamic potentials, entropy, free energy, chemical potentials, Maxwell relations, the Gibbs–Duhem equation, and response functions. All quantities stem from a single free-energy formalism, ensuring internal consistency and adherence to thermodynamic laws. This is crucial for building reliable EOS tables that can be used in simulations without introducing inconsistencies.

The relativistic mean-field model is developed to maintain thermodynamic consistency by factoring in rearrangement effects from density-dependent coupling constants. The formulation respects conservation laws, preserves causality and stability across the relevant densities, and delivers a coherent description of nuclear matter from below saturation to well above nuclear density. This framework sets the stage for accurate and consistent modeling in neutron star research.

The framework is intended to support high-impact studies in neutron-star structure, multimessenger astrophysics, and nuclear theory. We provide appendices with full derivations, analytic integrals, and runnable pseudocode to facilitate adoption.

Acknowledgments

I would like to express my sincere gratitude to **Professor Khanna** for his invaluable guidance, insightful discussions, and significant contributions to the theoretical development of this research, particularly in the derivation of the governing equations and the interpretation of relativistic many-body physics relevant to dense nuclear matter. I am also deeply grateful to **Professor Roich** for his valuable contributions to the derivation of key mathematical formulations, careful editing of the manuscript, and meticulous proofreading, which greatly enhanced the scientific rigor, clarity, and overall quality of this work. Their expertise, constructive comments, and unwavering encouragement have been instrumental in the successful completion of this research. Any remaining errors or omissions are entirely my own responsibility.

Data availability and reproducibility

All pseudocode, sample EOS tables, and scripts to reproduce the illustrative results are provided in the supplementary material (code repository link to be inserted by authors). The pipeline is modular and designed for translation to Python/Fortran/C++ with double precision arithmetic. For production EOSs, use published RMF parameter sets (e.g., NL3, DD2) and include full calibration against nuclear data.

Suggested further reading

Readers seeking background on RMF theory, neutron-star EOSs, neutrino opacities, and sensitivity analysis may consult standard texts and recent reviews in nuclear astrophysics and statistical UQ.

References

[1] Akita, K., & Yamaguchi, M. (2020). A precision calculation of relic neutrino decoupling. *Journal of Cosmology and Astroparticle Physics*, *2020*(08), 012–012.

[2] Aldulaimi, S. M., & Alzubadi, A. A. (2024). Nuclear Structure Study Using Relativistic Mean Field (RMF) Method. *Iraqi Journal of Physics*, *22*(4), 21–41.

[3] Beznogov, M. V., & Raduta, A. R. (2023). Bayesian inference of the dense matter equation of state built upon covariant density functionals. *Physical Review C*, *107*(4), 045803.

[4] Borgnakke, C. (2025). *Fundamentals of thermodynamics*. John Wiley & Sons.

[5] Brooks, S., Gelman, A., Jones, G., & Meng, X.-L. (2011). *Handbook of markov chain monte carlo*. CRC press.

[6] Cai, B.-J., Li, B.-A., & Ma, Y.-G. (2026). Nucleon short-range correlations and high-momentum dynamics: Implications on the equation of state of dense matter. *The European Physical Journal Special Topics*, 1–137.

[7] Chaparro, G., & Müller, E. A. (2024). Development of a Helmholtz free energy equation of state for fluid and solid phases via artificial neural networks. *Communications Physics*, *7*(1), 406.

[8] Costa, P., Pereira, R. C., & Providência, C. (2020). Role of the conserved charges in the chiral symmetry restoration phase transition. *Physical Review D*, *102*(5), 054010.

[9] Cruz-Camacho, N., Conde-Ocazionez, C., Dexheimer, V., Noronha-Hostler, J., & Yunes, N. (2026). Sensitivity of neutron star observables to microscopic nuclear parameters of realistic equations of state. *arXiv Preprint arXiv:2603.16019*.

[10] Dwibedi, A., Padhan, N., Chatterjee, A., & Ghosh, S. (2024). Transport coefficients of relativistic matter: A detailed formalism with a gross knowledge of their magnitude. *Universe*, *10*(3), 132.

[11] Fischer, T. (2016). The role of medium modifications for neutrino-pair processes from nucleon-nucleon bremsstrahlung-Impact on the protoneutron star deleptonization. *Astronomy & Astrophysics*, *593*, A103.

[12] Fischer, T., Guo, G., Martínez-Pinedo, G., Liebendörfer, M., & Mezzacappa, A. (2020). Muonization of supernova matter. *Physical Review D*, *102*(12), 123001.

[13] Frohaug, G., Maslov, K., Dexheimer, V., Grefa, J., Jahan, J., Ratti, C., & Restrepo, T. E. (2026). Relativistic mean-field model with density-and isospin-density-dependent couplings. *Physical Review D*, *113*(12), 123049.

[14] Goimil-García, M., Shalgar, S., & Tamborra, I. (2025). Pauli blocking: Probing beyond-mean-field effects in neutrino flavor evolution. *Physical Review D*, *111*(8), 083054.

[15] Guerrini, M. (2026). *Deconfinement phase transition in dense matter and its effects on the formation of compact stars*.

[16] Huber, M. L., Lemmon, E. W., Bell, I. H., & McLinden, M. O. (2022). The NIST REFPROP database for highly accurate properties of industrially important fluids. *Industrial & Engineering Chemistry Research*, *61*(42), 15449–15472.

[17] Kalies, G., & Do, D. D. (2023). Momentum work and the energetic foundations of physics. IV. The essence of heat, entropy, enthalpy, and Gibbs free energy. *AIP Advances*, *13*(9).

[18] Kara, S. (2025a). Leptophilic Interactions in Nuclear Energy Density Functional Theory. *arXiv Preprint arXiv:2512.11770*.

[19] Kara, S. (2025b). Leptophilic Interactions in Nuclear Energy Density Functional Theory. *arXiv Preprint arXiv:2512.11770*.

[20] Kasza, G., Takátsy, J., & Wolf, G. (2026). Astrophysical constraints on the cold equation of state of the strongly interacting matter. *The European Physical Journal Special Topics*, 1–15.

[21] Koffa, D., Ogunjobi, O., Omonile, J., Obaje, V., Ahmed Ade, F., Aliyu, N., & Olorunleke, I. (2025). Computational framework for quantum gravity phenomenology: Numerical methods and future observational prospects in multi-messenger astrophysics. *Journal of Basics and Applied Sciences Research*, *3*(4), 166–172.

[22] Lee, J. H., & Ramamurthi, K. (2022). *Fundamentals of thermodynamics*. CRC Press.

[23] Lukáčová-Medvid'ová, M., Thein, F., Warnecke, G., & Yuan, Y. (2025). A note on relations between convexity and concavity of thermodynamic functions. *arXiv Preprint arXiv:2510.24440*.

[24] Luz, P. (2026). Series solutions to the Tolman-Oppenheimer-Volkoff equations. *Physical Review D*, *114*(2), 024003.

[25] Maruyama, T., Tatsumi, T., Voskresensky, D. N., Tanigawa, T., & Chiba, S. (2005). Nuclear "pasta" structures and the charge screening effect. *Physical Review C—Nuclear Physics*, *72*(1), 015802.

[26] McClarren, R. G. (2021). Two-group radiative transfer benchmarks for the non-equilibrium diffusion model. *Journal of Computational and Theoretical Transport*, *50*(6–7), 583–597.

[27] Mendes, M., & Lenzi, C. H. (2026). Reconciling GW170817 and GW190814 with a Nonmonotonic Sound-Speed Equation of State. *arXiv Preprint arXiv:2605.30369*.

[28] Miyatsu, T., Cheoun, M.-K., & Saito, K. (2022). Asymmetric nuclear matter in relativistic mean-field models with isoscalar-and isovector-meson mixing. *The Astrophysical Journal*, *929*(1), 82.

[29] Musolino, C., & Rezzolla, L. (2024). A practical guide to a moment approach for neutrino transport in numerical relativity. *Monthly Notices of the Royal Astronomical Society*, *528*(4), 5952–5971.

[30] Neukart, F., & Vinokur, V. (2025). Thermodynamic-Complexity Duality: Embedding Computational Hardness as a Thermodynamic Coordinate. *arXiv Preprint arXiv:2501.15950*.

[31] Nikiforov, A. F., Novikov, V. G., & Uvarov, V. B. (2005). *Quantum-statistical models of hot dense matter: Methods for computation opacity and equation of state*. Springer.

[32] Schuetrumpf, B., Martínez-Pinedo, G., Afibuzzaman, M., & Aktulga, H. M. (2019). Survey of nuclear pasta in the intermediate-density regime: Shapes and energies. *Physical Review C*, *100*(4), 045806.

[33] Xie, W.-J., & Xia, C.-J. (2026). Inverse-mapped density-dependent relativistic mean-field inference of the neutron-star equation of state with multi-messenger constraints. *arXiv Preprint arXiv:2603.06128*.

[34] 이세혁. (2019). *Bayesian Frameworks for Probabilistic System Identification of Structural Parameters*.